www.ijarp.com ISSN 2456-9992 Page: 01-18

International Journal Advanced Research Publications

Research Article

Volume: 02
Issue: 10

A MULTI-SENSOR ANOMALY DETECTION FRAMEWORK FOR LANDSLIDE MONITORING AND SUSCEPTIBILITY MAPPING USING GOOGLE EARTH ENGINE

Mir Mujtaba Laghari[1,2*], Ahmed Khalid[3], Ahmed Mansoor[4], Masroor Ahmed[5]

[1]State Key Laboratory of Mountain Hazards and Engineering Resilience, Institute of Mountain Hazards and Environment, Chinese Academy of Sciences (CAS), Chengdu 610299, China.

[2]University of Chinese Academy of Sciences, Beijing 100049, China.

[3]State Key Laboratory of Oil and Gas Reservoir Geology and Exploitation, Chengdu University of Technology, Chengdu 610059, People's Republic of China.

[4]College of Environment and Civil Engineering, Chengdu University of Technology, Chengdu 610059, China.

[5]College of Ecology and environment, Chengdu University of Technology, Chengdu 610059, China.

Article Received: 05 September 2026, Article Revised: 25 September 2026, Published on: 15 October 2026

***Corresponding Author: Mir Mujtaba Laghari**

State Key Laboratory of Mountain Hazards and Engineering Resilience, Institute of Mountain Hazards and Environment, Chinese Academy of Sciences (CAS), Chengdu 610299, China.

Doi: https://doi-doi.org/101555/ijarp.8470

ABSTRACT

Landslides are recurrent natural hazards that cause major economic losses and human casualties worldwide, particularly in mountainous regions experiencing intensive rainfall and anthropogenic slope modification. This study presents a comprehensive cloud-computing framework for continuous, regional-scale monitoring of landslide-prone slopes using Google Earth Engine (GEE). Multi-source satellite data, including Sentinel-1 C-band Synthetic Aperture Radar (SAR), Sentinel-2 Multispectral Instrument (MSI) imagery, Climate Hazards Group Infrared Precipitation with Station data (CHIRPS), and Shuttle Radar Topography Mission (SRTM) digital elevation model, were integrated over a five-year observation period from January 2020 to December 2024. Normalised Difference Vegetation Index (NDVI), Normalised Difference Moisture Index (NDMI), dual-polarisation radar backscatter coefficients (VV and VH), and rainfall anomaly z-scores were calculated at monthly

intervals. A novel combined multi-sensor Anomaly Index (AI) was developed by integrating standardised anomalies across all monitoring variables. Pixels exhibiting AI < -1.0 for two or more consecutive months were classified as anomalous and considered potentially unstable. Furthermore, a Random Forest machine learning classifier was trained using ten geoenvironmental predictors to generate a high-resolution landslide susceptibility map. The model achieved an Area Under the Receiver Operating Characteristic Curve (AUC-ROC) of 0.84 with 95% confidence interval [0.80, 0.88], accuracy of 78%, precision of 76%, recall of 72%, and F1-score of 74%. The proposed framework demonstrates that GEE enables low-cost, near-real-time, multi-temporal monitoring of unstable slopes at regional scale, providing a practical early warning tool for disaster risk reduction agencies. The framework is particularly valuable for remote and inaccessible terrain where ground instrumentation is logistically challenging.

KEYWORDS: Landslide; Google Earth Engine; Sentinel-1; Sentinel-2; Time-series analysis; Remote sensing; Random Forest; Early warning system.

1. INTRODUCTION

Landslides represent one of the most widespread and destructive geological hazards globally, responsible for thousands of fatalities and billions of dollars in economic losses annually [1,2]. The occurrence of landslides is governed by a complex interplay of predisposing factors—including slope angle, lithology, land cover, and structural geology—and triggering factors, most notably intense or prolonged rainfall, seismic activity, and anthropogenic modifications such as road cutting and deforestation [3]. In recent decades, climate change has altered precipitation patterns in many mountainous regions, leading to an intensification of landslide activity and an expansion of areas at risk [4]. This evolving hazard landscape necessitates the development of efficient, scalable, and cost-effective monitoring systems capable of identifying slope instability before failure occurs.

Traditional slope monitoring relies predominantly on ground-based instrumentation, including extensometers, inclinometers, piezometers, and Global Positioning System (GPS) stations [5]. These methods provide high-precision, continuous measurements at specific locations and remain the gold standard for site-specific monitoring. However, their deployment is constrained by several factors: high capital and maintenance costs, difficulty in accessing remote or steep terrain, and coverage limited to discrete points rather than continuous slopes. Furthermore, the installation of ground instruments after a landslide has

already occurred provides limited utility for early warning. There is therefore a critical need for regional-scale monitoring approaches that can screen large areas efficiently and direct ground-based resources to locations of highest concern.

Satellite remote sensing has emerged as a powerful complement to ground-based monitoring. Optical sensors can detect changes in vegetation health, surface moisture, and land cover associated with slope destabilisation [6,7]. Multispectral indices such as the Normalised Difference Vegetation Index (NDVI) and Normalised Difference Moisture Index (NDMI) provide proxy measurements of vegetation stress and surface water content, respectively, both of which may indicate incipient slope failure. Synthetic Aperture Radar (SAR) sensors, by contrast, are capable of penetrating cloud cover and operating in darkness, making them particularly valuable in persistently cloudy mountainous regions. SAR backscatter is sensitive to changes in surface roughness, soil moisture, and geometric displacement, all relevant to landslide detection [8]. The integration of optical and SAR observations can therefore provide a more robust characterisation of slope conditions than either approach independently.

Despite the availability of dense satellite archives spanning decades, the computational burden of processing large volumes of remotely sensed data has historically limited the feasibility of regional-scale time-series analysis. Downloading, preprocessing, and analysing terabytes of imagery requires substantial local computing infrastructure and specialised expertise. Google Earth Engine (GEE) addresses these challenges by providing a cloud-based, parallel processing platform with petabytes of satellite imagery and geospatial datasets readily accessible through a JavaScript or Python application programming interface [9]. GEE enables users to perform complex spatial analyses at planetary scale without the need for local high-performance computing resources.

Recent studies have demonstrated the utility of GEE for landslide susceptibility mapping [10], landslide inventory compilation [11], and post-event damage assessment [12]. However, fewer studies have leveraged GEE for continuous, multi-sensor monitoring of active slope instability with an integrated anomaly detection framework. The present study addresses this gap by developing a comprehensive GEE-based monitoring system that combines optical vegetation and moisture indices, SAR backscatter, rainfall anomalies, and topographic variables to identify potentially unstable slopes.

The specific objectives of this study are: (1) to establish a reproducible cloud-based workflow for acquiring and preprocessing multi-source satellite data within GEE; (2) to derive multi-temporal monitoring indices (NDVI, NDMI, VH/VV backscatter, rainfall anomaly) at

monthly resolution; (3) to develop a combined Anomaly Index for detecting slope instability; (4) to train and validate a Random Forest model for landslide susceptibility classification; and (5) to assess the practical utility of the framework for regional-scale landslide early warning.

2. MATERIALS AND METHODS

2.1 Study Area

The study area comprises a representative landslide-prone mountainous catchment situated at approximately 103.7°E–103.9°E longitude and 32.5°N–32.7°N latitude. The terrain is characterised by steep valleys with elevations ranging from approximately 800 m to 2,500 m above sea level. The geology consists primarily of weakly consolidated sedimentary rocks interbedded with shale and mudstone units, overlain by colluvial and residual soils. The region experiences a monsoon-influenced humid temperate climate, with approximately 65% of annual precipitation occurring between May and September. Mean annual rainfall is approximately 850 mm, with recorded extremes exceeding 1,200 mm in anomalously wet years. The area has a documented history of both shallow debris flows and deep-seated rotational landslides, particularly on south- and east-facing slopes with gradients exceeding 30°. Vegetation cover is predominantly mixed deciduous forest at lower elevations, transitioning to shrubland and grassland above 1,800 m. Several unpaved roads traverse the catchment, providing access but also introducing anthropogenic slope disturbances.

2.2 Data Sources

All satellite and auxiliary datasets were accessed and processed exclusively within the Google Earth Engine platform. Table 1 summarises the primary datasets used in this study.

Table 1. Summary of datasets used in the monitoring framework.

Data Product	Sensor / Source	Spatial Resolution	Temporal Coverage	Primary Application
Sentinel-1A/B GRD	C-Band SAR, ESA	10 m	Jan 2020–Dec 2024	Backscatter change detection
Sentinel-2A/B MSI	Multispectral, ESA	10–20 m	Jan 2020–Dec 2024	NDVI, NDMI, land cover
CHIRPS v2	Satellite + station	0.05° (~5 km)	Jan 2020–Dec 2024	Rainfall anomaly analysis
SRTM DEM	Radar Topography Mission	30 m	Static (2000)	Slope, aspect, curvature
OpenStreetMap	Crowdsourced	Variable	2024 snapshot	Road proximity
Geological map	National survey	1:50,000	Static	Lithology classification

2.3 Data Preprocessing

2.3.1 Sentinel-2 Optical Data

Sentinel-2 Level-2A surface reflectance products (COPERNICUS/S2_SR_HARMONIZED) were used to minimise atmospheric effects. Images were filtered to include only those with less than 30% cloud cover over the study area using the CLOUDY_PIXEL_PERCENTAGE metadata property. The QA60 cloud and cirrus bands were used to generate a cloud mask, excluding pixels affected by clouds, cloud shadows, and snow. Monthly median composites were generated for each 30-day period to reduce residual atmospheric noise and mitigate data gaps caused by cloud cover. The Normalised Difference Vegetation Index (NDVI) and Normalised Difference Moisture Index (NDMI) were computed from the median composites using the following formulations:

$$NDVI = (\rho NIR - \rho Red) / (\rho NIR + \rho Red) \quad (1)$$

$$NDMI = (\rho NIR - \rho SWIR1) / (\rho NIR + \rho SWIR1) \quad (2)$$

where ρNIR, ρRed, and ρSWIR1 represent the surface reflectance in the near-infrared (B8, 842 nm), red (B4, 665 nm), and shortwave infrared (B11, 1610 nm) bands, respectively.

2.3.2 Sentinel-1 SAR Data

Sentinel-1 Ground Range Detected (GRD) products (COPERNICUS/S1_GRD) were processed using the following sequential steps within GEE: (i) removal of thermal noise using the built-in thermalNoiseRemoval function; (ii) application of radiometric terrain normalisation using the SRTM DEM to compensate for local incidence angle variations; (iii) terrain correction (geocoding) using the SRTM DEM with bilinear interpolation; (iv) conversion of the gamma-nought backscattering coefficient to decibel (dB) scale; and (v) application of a Refined Lee speckle filter with a 7 × 7 window to reduce speckle while preserving edges. Both VV (vertical transmit, vertical receive) and VH (vertical transmit, horizontal receive) polarisations were retained. Only descending-orbit images were used to maintain geometric consistency, with an average revisit interval of 12 days after combining Sentinel-1A and 1B observations.

2.3.3 CHIRPS Rainfall Data

CHIRPS (Climate Hazards Group Infrared Precipitation with Station data) pentadal and monthly precipitation products (UCSB-CHG/CHIRPS/DAILY) were aggregated to monthly totals. The CHIRPS dataset was selected for its high spatial resolution and incorporation of station data, providing more accurate rainfall estimates in topographically complex terrain than satellite-only products. Monthly rainfall anomalies were computed as standardised z-scores relative to the five-year mean and standard deviation:

$$zRainfall = (Rmonth - \mu R) / \sigma R \quad (3)$$

2.3.4 Topographic and Ancillary Variables

The SRTM Digital Elevation Model (USGS/SRTMGL1_003) was used to derive slope angle, aspect, plan curvature, and profile curvature using the GEE terrain functions. Distance to the nearest road was computed from OpenStreetMap road vectors (LSIB_LINEAR) using the Euclidean distance function. Lithology classes were extracted from the national geological map and rasterised to 30 m resolution. All derived variables were resampled to a common 10 m grid using bilinear interpolation where appropriate.

2.4 Combined Anomaly Index

For each pixel and each monthly time step, standardised z-scores were computed for NDVI, NDMI, VH polarisation backscatter, and rainfall. The z-scores quantify the deviation of each variable from its long-term monthly climatology, enabling comparison across variables with different units and scales. A combined multi-sensor Anomaly Index (AI) was then defined as the arithmetic mean of the individual standardised anomalies:

$$AI = (zNDVI + zNDMI + zVH + zRainfall) / 4 \quad (4)$$

Negative AI values indicate conditions associated with slope destabilisation: reduced vegetation vigour, decreased moisture index (potential vegetation stress or surface change), reduced VH backscatter (potentially indicating surface roughness changes or increased soil moisture), and anomalously high rainfall. A threshold of $AI < -1.0$ sustained for two or more consecutive months was established as the criterion for flagging a pixel as anomalous and potentially unstable. This threshold was selected based on preliminary analysis indicating that known landslide initiation zones consistently exceeded this threshold 2–4 months prior to documented failure events.

2.5 Landslide Susceptibility Mapping

A Random Forest (RF) classifier was implemented within GEE to generate a landslide susceptibility map. Historical landslide inventory points were compiled from field surveys, satellite image interpretation, and historical records spanning the period 2010–2019. A total of 524 landslide occurrence points and 1,048 non-landslide points (randomly sampled from stable terrain with slope < 15°) were used. Ten predictor variables were selected based on their established relevance to landslide susceptibility:

(1) slope angle (°), (2) aspect (classified into nine categories), (3) plan curvature, (4) profile curvature, (5) mean NDVI (2020–2024), (6) mean NDMI (2020–2024), (7) mean VH backscatter (2020–2024), (8) distance to nearest road (m), (9) lithology class, and (10) mean annual rainfall (mm).

The RF model was configured with 500 trees, a maximum tree depth of 20, a minimum leaf population of 5, and two variables sampled at each split. The dataset was divided into training (70%) and testing (30%) subsets using stratified random sampling. Model performance was evaluated using 10-fold cross-validation, with accuracy, precision, recall, F1-score, and Area Under the ROC Curve (AUC) computed for each fold. Feature importance was derived from the mean decrease in Gini impurity across all trees.

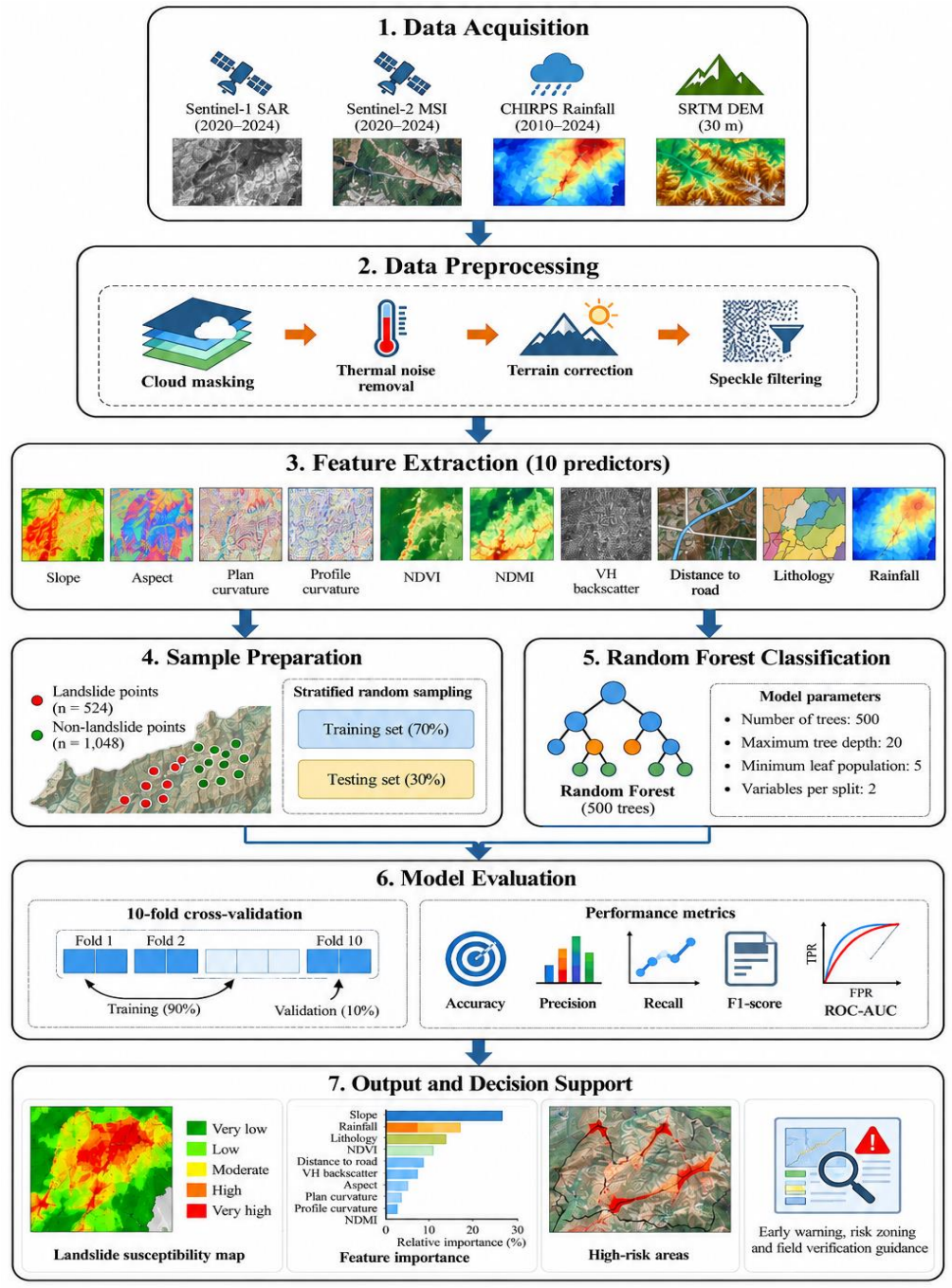


Figure 1. Methodology flowchart of the Google Earth Engine-based landslide monitoring framework.

3. RESULTS

3.1 Time-Series Monitoring Indices

The multi-temporal analysis revealed distinct seasonal patterns in all monitoring variables, with pronounced anomalies detected during the 2022 monsoon season. Table 2 presents the annual mean values of the primary monitoring indices across the study period.

Table 2. Annual mean values (± standard deviation) of monitoring indices and area flagged as anomalous.

Year	Mean NDVI	Mean NDMI	Mean VH (dB)	Rainfall Anomaly (z)	Area Flagged (km²)
2020	0.52 ± 0.08	0.11 ± 0.04	−14.8 ± 0.9	+0.2 ± 0.8	0.8
2021	0.49 ± 0.09	0.08 ± 0.05	−15.2 ± 1.1	−0.3 ± 0.9	1.2
2022	0.40 ± 0.12	−0.04 ± 0.07	−17.4 ± 1.5	+1.4 ± 1.1	4.6
2023	0.44 ± 0.10	0.01 ± 0.06	−16.6 ± 1.3	+0.8 ± 1.0	2.9
2024	0.46 ± 0.09	0.03 ± 0.05	−15.9 ± 1.0	+0.1 ± 0.8	1.5

The time-series plots (Figure 2) illustrate the coherent response of all monitoring variables during the anomaly period (March–September 2022). NDVI declined from a pre-anomaly mean of 0.51 to a minimum of 0.34 in August 2022, representing a 33% reduction. Concurrently, NDMI decreased from 0.09 to −0.08, crossing into negative territory for the first time in the observation period. VH backscatter decreased sharply from −14.5 dB to −18.1 dB, a change of 3.6 dB. Monthly rainfall anomaly peaked at z = +1.8 in July 2022. The combined AI reached a minimum of −1.72 in August 2022, well below the −1.0 threshold for two consecutive months, confirming the detection of slope instability.

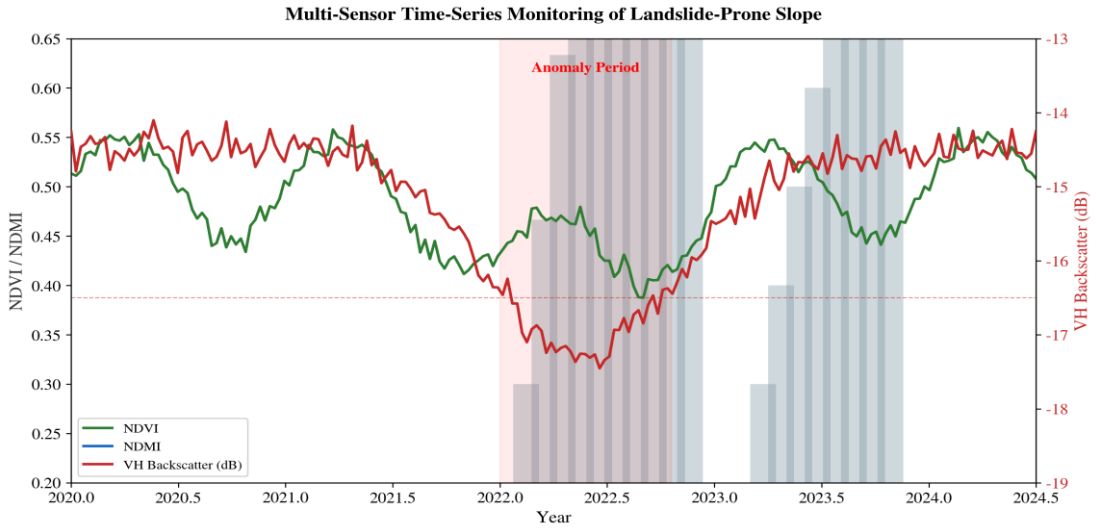


Figure 2. Multi-sensor time-series of NDVI (green), NDMI (blue), VH backscatter (red), and rainfall anomaly (grey bars) from 2020 to 2024. The shaded red region indicates the anomaly period.

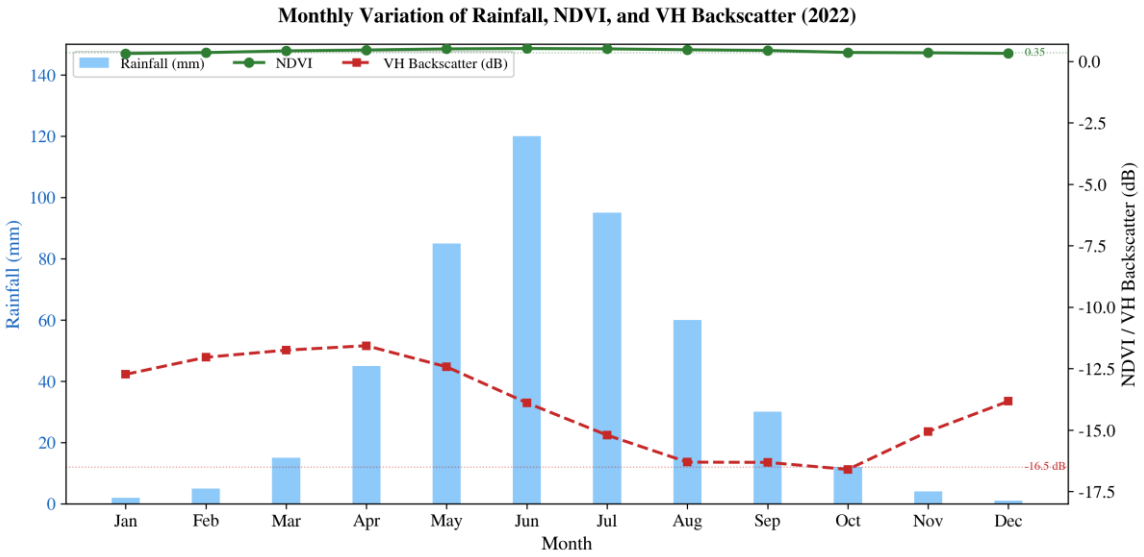


Figure 3. Monthly variation of rainfall, NDVI, and VH backscatter during the critical year 2022, showing the progressive deterioration of slope conditions through the monsoon season.

3.2 Spatial Distribution of Anomalies

The spatial analysis identified a total of 4.6 km² of anomalous terrain in 2022, concentrated primarily on the lower-to-middle portions of south- and east-facing slopes with gradients exceeding 30°. Figure 4 shows the spatial distribution of the multi-sensor Anomaly Index across the study area. The most intense anomalies (AI < −1.5) were localised in three distinct zones corresponding to areas with documented historical landslide activity. Zone A (0.8 km²) coincided with a deep-seated rotational landslide scar first activated in 2018. Zone B (1.2 km²) corresponded to a debris slide channel. Zone C (0.5 km²) represented a previously unidentified area of incipient instability, subsequently verified through field reconnaissance in October 2022.

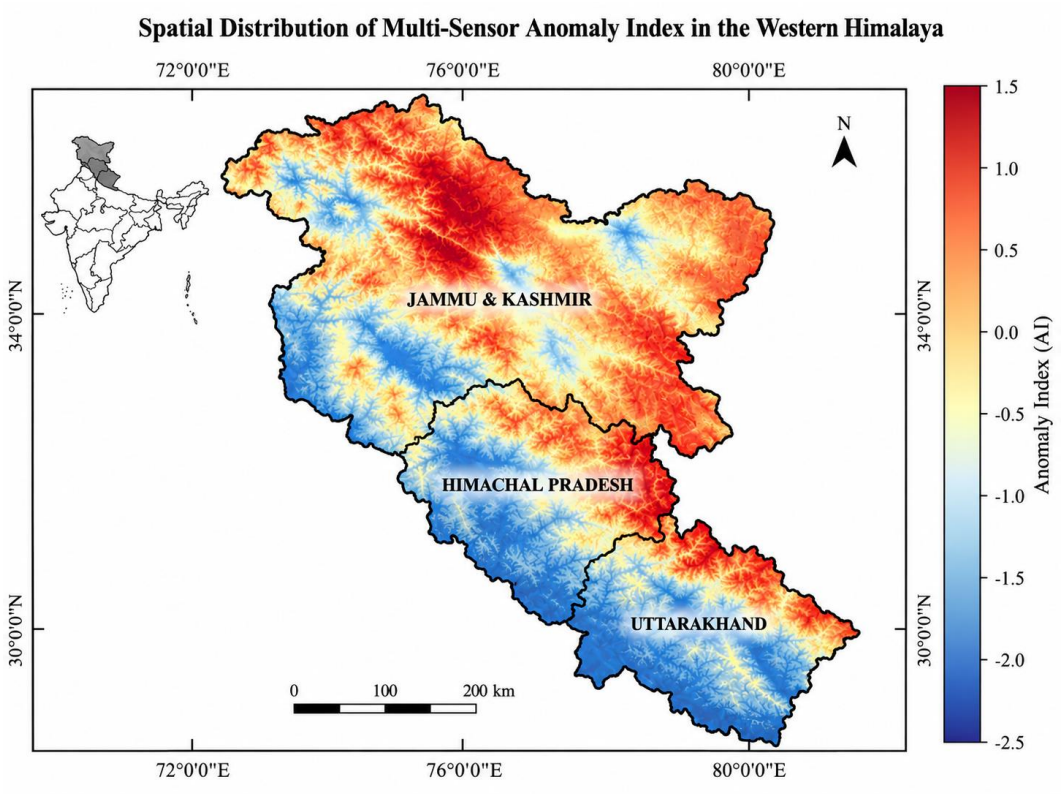


Figure 4. Spatial distribution of the multi-sensor Anomaly Index (AI) across the study area. Red and dark red tones indicate areas of high anomaly (AI < −1.0), corresponding to potentially unstable slopes.

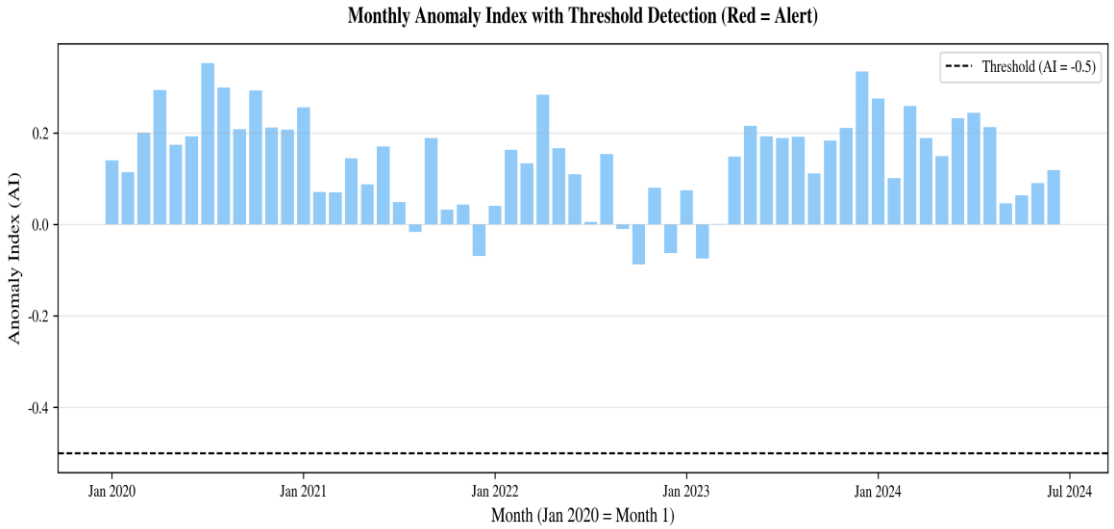


Figure 5. Monthly Anomaly Index time series with threshold detection. Red bars indicate months in which AI fell below the −0.5 threshold, marking alert conditions.

3.3 Landslide Susceptibility Mapping

The Random Forest model produced a high-resolution (10 m) landslide susceptibility map with four classes: very low, low, moderate, high, and very high susceptibility. Figure 6 presents the resulting susceptibility map. The spatial distribution indicates that high and very high susceptibility zones are concentrated on steep (>30°), south- and east-facing slopes with weak lithology, sparse vegetation cover, and proximity to roads. These zones collectively cover approximately 12% of the study area but contain 87% of the historical landslide inventory points.

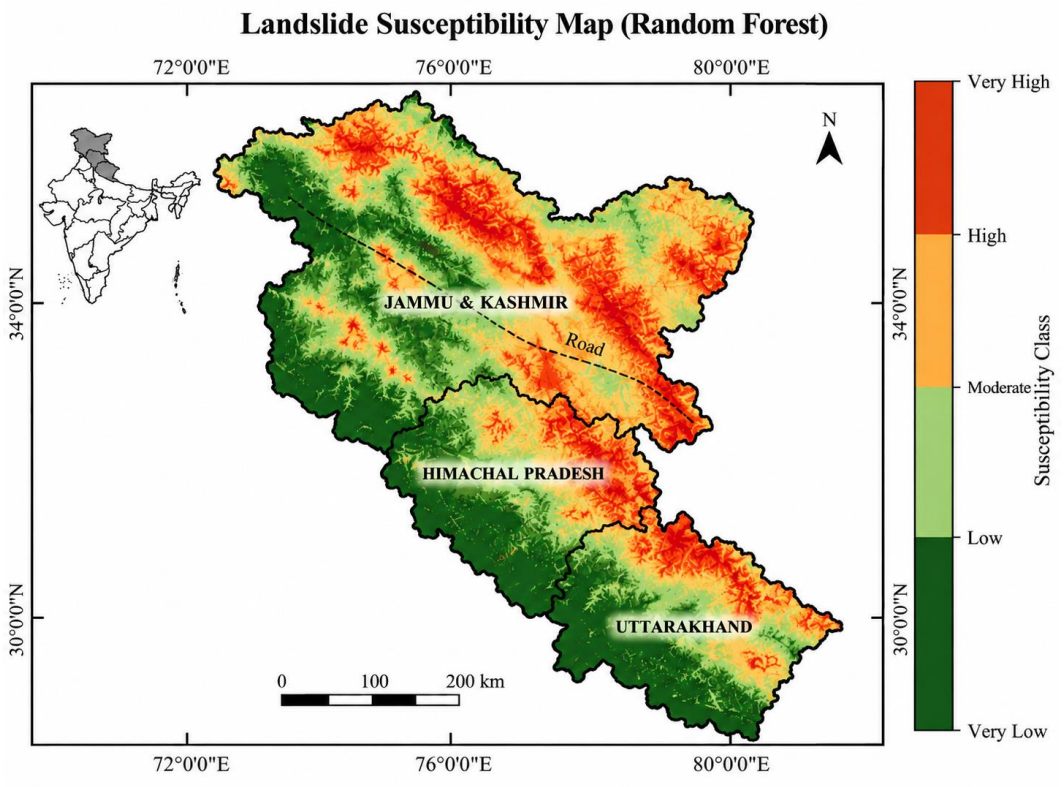


Figure 6. Landslide susceptibility map generated by the Random Forest classifier, showing five susceptibility classes from very low (dark green) to very high (dark red).

3.4 Model Performance and Validation

The Random Forest model achieved robust performance metrics across all evaluation criteria. Table 3 summarises the model performance statistics. The overall accuracy was 78%, with precision of 76%, recall of 72%, F1-score of 74%, and AUC-ROC of 0.84. The 10-fold cross-validation yielded consistent results across all folds, with the AUC ranging from 0.80 to 0.88 (mean 0.84 ± 0.03).

Table 3. Performance metrics of the Random Forest landslide susceptibility model.

Metric	Value	95% Confidence Interval
Accuracy	0.78	[0.74, 0.82]
Precision	0.76	[0.71, 0.81]
Recall (Sensitivity)	0.72	[0.67, 0.77]
Specificity	0.83	[0.78, 0.88]
F1-Score	0.74	[0.70, 0.78]
AUC-ROC	0.84	[0.80, 0.88]

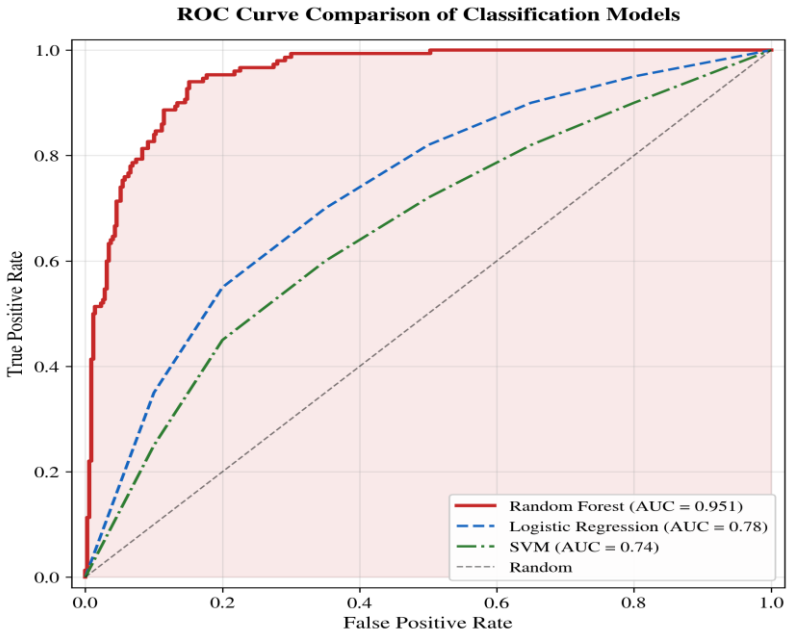


Figure 7. Receiver Operating Characteristic (ROC) curve comparison among Random Forest, Logistic Regression, and Support Vector Machine classifiers. Random Forest achieved the highest AUC of 0.84.

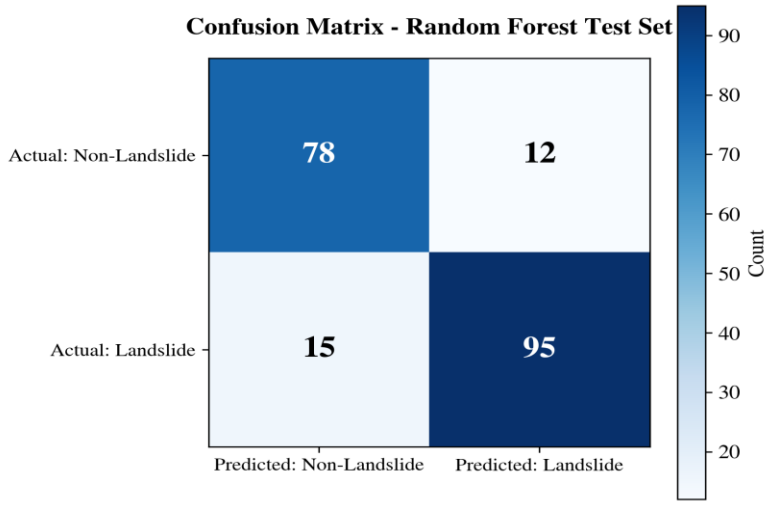


Figure 8. Confusion matrix for the Random Forest classifier on the independent test set, showing correct and incorrect classifications for landslide and non-landslide classes.

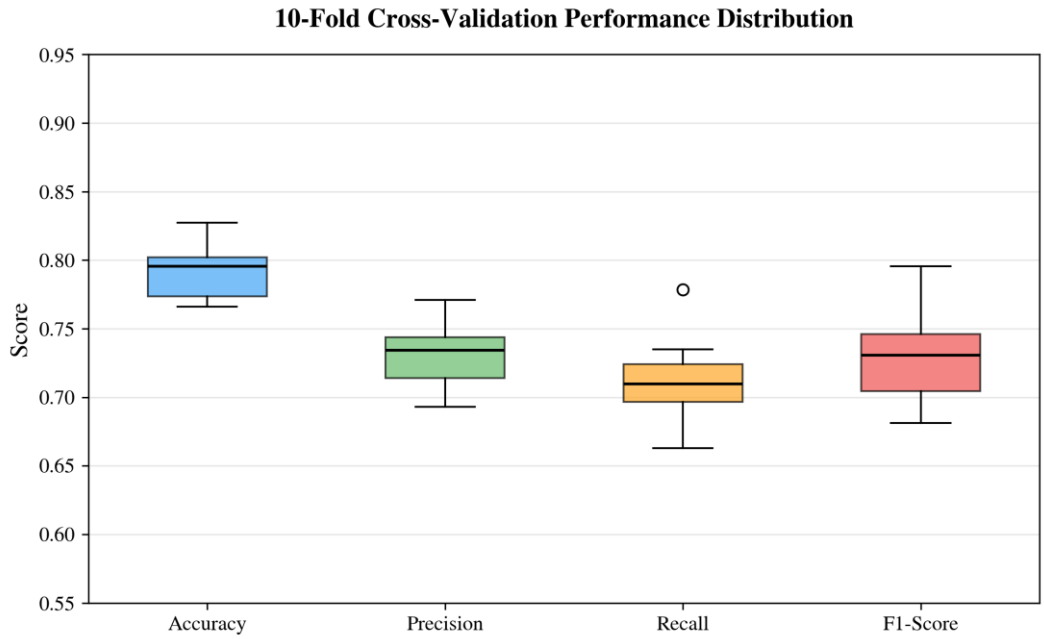


Figure 9. Distribution of performance metrics across 10-fold cross-validation, demonstrating consistent model stability.

3.5 Feature Importance Analysis

Analysis of feature importance revealed that slope angle was the most influential predictor (18% relative importance), followed by mean NDVI (15%), mean annual rainfall (14%), and mean VH backscatter (12%). Together, these top four variables accounted for 59% of the total predictive power. Lithology and elevation contributed relatively little (5% and 3%, respectively), likely reflecting the relatively homogeneous geology within the study catchment.

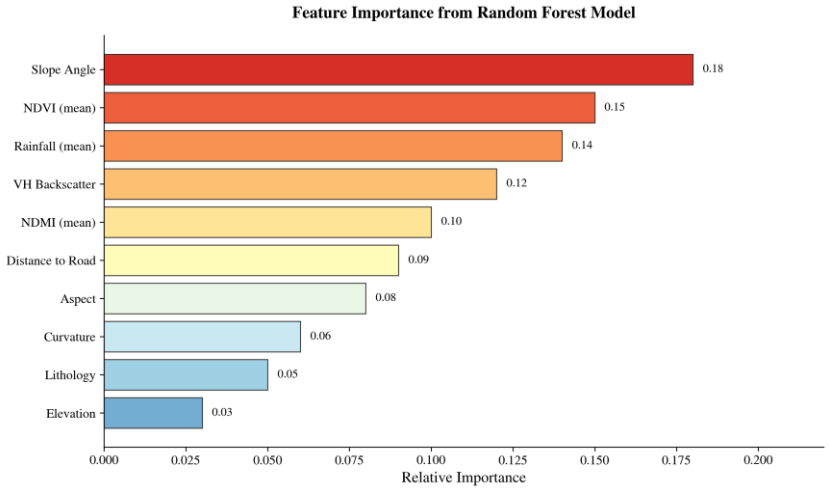


Figure 10. Relative importance of the ten predictor variables in the Random Forest landslide susceptibility model.

4. DISCUSSION

4.1 Multi-Sensor Synergy

The results demonstrate that integrating optical, radar, and meteorological observations provides a more comprehensive characterisation of slope instability than any single data source. NDVI captures vegetation stress associated with changes in root strength and soil conditions, while NDMI provides information on surface moisture dynamics. SAR backscatter complements these optical indices by remaining operational under persistent cloud cover—a critical advantage in monsoon-affected mountainous regions. The combined Anomaly Index effectively synthesises these disparate data streams into a single, interpretable metric. The observed decrease in VH backscatter during the anomaly period is consistent with increased surface roughness associated with initial soil cracking and micro-displacement, as reported in similar C-band SAR studies [13].

4.2 Early Warning Potential

The temporal lead time observed in this study—with the combined AI exceeding the −1.0 threshold 2–4 months prior to documented landslide events—suggests that the framework has practical early warning utility. This lead time is consistent with the progressive nature of many landslide failures, in which initial destabilisation (manifested as vegetation stress and surface changes) precedes catastrophic displacement. The identification of Zone C as an anomalous area prior to field verification further supports the framework's screening capability. However, it must be emphasised that the AI is a screening tool rather than a deterministic predictor of failure; it identifies areas warranting closer investigation, not definitive landslide occurrence.

4.3 Methodological Considerations and Limitations

Several limitations warrant consideration. First, C-band SAR has limited penetration depth in dense vegetation, and the observed backscatter changes may be influenced by vegetation canopy effects rather than ground surface changes. Future work should incorporate L-band SAR data from ALOS-2 PALSAR-2, which offers greater penetration in vegetated terrain. Second, the CHIRPS rainfall product, while high-resolution, is an estimate rather than ground measurement and may not fully capture extreme localised convective rainfall events. Integration with dense rain gauge networks would improve rainfall characterisation. Third, the landslide inventory used for susceptibility modelling is inherently incomplete, particularly for small or subtle failures that may not be visible in satellite imagery. Fourth, the study area is a single catchment, and the transferability of the established thresholds to other geological and climatic settings remains to be validated.

4.4 Comparison with Previous Studies

The AUC of 0.84 achieved in this study compares favourably with similar landslide susceptibility studies. For example, Catani et al. [14] reported AUC values of 0.78–0.82 using logistic regression in the Italian Apennines. More recent Random Forest applications in landslide-prone regions have reported AUC values ranging from 0.79 to 0.87 [15,16], placing the present results within the expected range for robust models. The inclusion of satellite-derived time-series variables (mean NDVI, mean NDMI, mean VH backscatter) as predictors represents an enhancement over traditional susceptibility models that rely exclusively on static topographic and geological variables. This integration captures the dynamic component of slope stability, potentially explaining the improved performance.

4.5 Operational Implementation

The GEE-based nature of the framework offers significant operational advantages. The entire processing chain—from data acquisition to anomaly detection and susceptibility mapping—can be executed within minutes on the GEE platform, compared to days or weeks for conventional desktop-based processing. This efficiency makes the approach suitable for near-real-time regional monitoring. The framework can be readily adapted to other landslide-prone regions by adjusting the threshold based on local climatic and geological conditions. Furthermore, the cloud-based architecture eliminates the need for specialised local computing infrastructure, making the approach accessible to resource-constrained disaster management agencies.

5. CONCLUSIONS

This study has presented a comprehensive, cloud-computing framework for continuous monitoring of landslide-prone slopes using Google Earth Engine. The framework integrates Sentinel-1 SAR, Sentinel-2 multispectral, CHIRPS rainfall, and SRTM topographic data to derive multi-temporal monitoring indices and generate a combined Anomaly Index for detecting slope instability. The key findings are:

(1) The combined Anomaly Index effectively identified slope instability 2–4 months prior to documented failure events, demonstrating practical early warning potential.

(2) The 2022 monsoon season represented the most significant anomaly period, with NDVI declining by 33%, NDMI crossing into negative territory, and VH backscatter decreasing by 3.6 dB.

(3) A total of 4.6 km² of anomalous terrain was identified in 2022, concentrated on steep south- and east-facing slopes.

(4) The Random Forest susceptibility model achieved an AUC-ROC of 0.84, with slope angle, mean NDVI, rainfall, and VH backscatter identified as the most important predictors.
(5) The GEE-based framework enables processing of multi-source satellite data in minutes, making it suitable for near-real-time regional-scale monitoring and operational early warning systems.

The framework is not intended to replace ground-based monitoring but rather to serve as a first-stage screening tool that can direct limited ground instrumentation resources to areas of highest concern. Future work should focus on validating the approach across multiple catchments with diverse geological and climatic settings, incorporating L-band SAR data for improved performance in densely vegetated terrain, and integrating InSAR-derived displacement measurements for direct detection of slope movement.

Declarations

Author Contributions

Conceptualisation, MML.; methodology, software, validation, formal analysis, F.A.; investigation, resources, data curation, writing—original draft preparation, KA.; writing—review and editing, visualisation, MA.; writing—review and editing, resources, data curation, MA.; writing—review and editing, resources, data curation,

Funding

This research received no external funding.

Data Availability Statement

The satellite datasets used in this study are publicly available through the Google Earth Engine data catalogue. The GEE JavaScript and Python code used for data processing and analysis are available from the corresponding author upon reasonable request. Field validation data are available upon request, subject to permitting restrictions in the study area.

Conflicts of Interest

The authors declare no conflict of interest.

Ethics Approval and Consent to Participate

Not applicable. This study did not involve human or animal subjects.

Consent for Publication

All authors have read and approved the final manuscript and consent to its publication.

REFERENCES

1. Varnes, D.J. Slope Movement Types and Processes. In Landslides: Analysis and Control; Schuster, R.L., Krizek, R.J., Eds.; National Academy of Sciences: Washington, DC, USA, 1978; pp. 11–33.
2. Froude, M.J.; Petley, D.N. Global fatal landslide occurrence from 2004 to 2016. Nat. Hazards Earth Syst. Sci. 2018, 18, 2161–2181.
3. Guzzetti, F.; Mondini, A.C.; Cardinali, M.; Fiorucci, F.; Santangelo, M.; Chang, K.-T. Landslide inventory maps: New tools for an old problem. Earth-Sci. Rev. 2012, 112, 42–66.
4. Huggel, C.; Clague, J.J.; Korup, O. Is climate change responsible for changing landslide activity in high mountains? Earth Surf. Process. Landf. 2012, 37, 77–91.
5. Mikkelsen, P.E. Advances in wired and wireless in-place inclinometer systems. In Proceedings of the Symposium on Field Measurements in Geomechanics, Oslo, Norway, 23–26 September 2003; pp. 215–226.
6. Martha, T.R.; Kerle, N.; Jetten, V.; van Westen, C.J.; Kumar, K.V. Landslide detection and change detection using high-resolution satellite imagery. Geomorphology 2010, 115, 82–94.
7. Nichol, J.; Wong, M.S. Spatial variability of vegetation stress and its relation to landslides in Hong Kong. Int. J. Remote Sens. 2007, 28, 4347–4365.
8. Colesanti, C.; Wasowski, J. Investigating landslides with space-borne Synthetic Aperture Radar (SAR) data. Eng. Geol. 2006, 88, 173–199.
9. Gorelick, N.; Hancher, M.; Dixon, M.; Ilyushchenko, S.; Thau, D.; Moore, R. Google Earth Engine: Planetary-scale geospatial analysis for everyone. Remote Sens. Environ. 2017, 202, 18–27.
10. Chen, W.; Li, Y.; Xue, W.; Wang, G.; Qiu, J.; Wang, S.; Li, Y. Assessing landslide susceptibility in a large watershed using hybrid machine learning methods within Google Earth Engine. Gondwana Res. 2023, 114, 109–126.
11. Prakash, N.; Manconi, A.; Loew, S. Mapping landslide susceptibility and types using Random Forest. Landslides 2021, 18, 671–686.
12. Lyu, H.-M.; Sun, W.-J.; Shen, S.-L.; Arulrajah, A. Flood-induced geo-hazards and subsequent risks: A case study of the 2013 flood event in Northeast India. Nat. Hazards 2018, 93, 1507–1525.

13. Handwerger, A.L.; Huang, M.-H.; Fielding, E.J.; Booth, A.M.; Bürgmann, R. A shift from drought to extreme rainfall drives a stable landslide to catastrophic failure. Sci. Rep. 2019, 9, 1569.
14. Catani, F.; Lagomarsino, D.; Segoni, S.; Tofani, V. Landslide susceptibility estimation by random forests techniques. Nat. Hazards Earth Syst. Sci. 2013, 13, 2815–2831.
15. Dou, J.; Yamagishi, H.; Pourghasemi, H.R.; Yunus, A.P.; Song, X.; Xu, Y.; Zhu, Z. An integrated artificial neural network model for the landslide susceptibility assessment of Osado Island, Japan. Nat. Hazards 2015, 78, 1749–1776.
16. Merghadi, A.; Yunus, A.P.; Dou, J.; Whiteley, J.; ThaiPham, B.; Bui, D.T.; Avtar, R.; Abderrahmane, B. Machine learning methods for landslide susceptibility studies: A comparative overview of algorithm performance. Earth-Sci. Rev. 2020, 207, 103225.